The Information Contained in Altimetric Sea Surface Height Frequency Spectra

CHARLY DE MAREZ[a] AND JÖRN CALLIES[b]

[a] *Háskóli Íslands, University of Iceland, Reykjavík, Ísland*
[b] *California Institute of Technology, Pasadena, California*

(Manuscript received 24 June 2024, in final form 2 December 2024, accepted 19 December 2024)

ABSTRACT: Despite the amount of data sampled by current and upcoming satellite missions, the temporal evolution of oceanic turbulence is for now poorly understood. Here, we use state-of-the-art satellite measurements of sea surface height time series, combined with global oceanic reanalysis and idealized numerical simulations to study the properties of the frequency spectrum for oceanic turbulence. We show that the meridional gradient of potential vorticity, that supports planetary Rossby waves, and the barotropic current are the main parameters that shape the frequency spectrum of sea surface height as observed by satellite altimetry.

KEYWORDS: Ocean; Turbulence; Satellite observations

1. Introduction

Oceanic currents with time scales larger than a day and length scales larger than tens of kilometers represent the major part of the oceanic circulation (Zhai et al. 2010; Beal et al. 2011; Zhang et al. 2014) and are essential for the evolution of climate (Small et al. 2008; Zhang et al. 2014; Palter 2015). The ubiquitous oceanic stratification implies that baroclinic instability injects energy at scales $\mathcal{O}(10-100)$ km, that subsequently cascades toward larger and smaller scales (Callies et al. 2016), forming the so-called turbulence continuum. Understanding the properties of this turbulence is of primary importance, from the large scale to the submesoscale, in order to understand the road from the astronomic forcing to the microscopic dissipation.

On the one hand, properties of the turbulence in the spatial domain (for wavenumbers k, averaged over all frequencies) are fairly well understood locally, but are challenging to measure at a global scale due to the noise floor and the entanglement of the different geophysical signals (Villas Bôas et al. 2022). The kinetic energy (KE) spectrum is predicted to follow a power law $\mathcal{K}(k) \propto k^{-\alpha}$ (e.g., Callies and Ferrari 2013), where k is a horizontal wavenumber. The slope α depends on the presence or absence of submesoscale instabilities and is thought to be shaped by the turbulent dynamics induced by a combination of these instabilities and the mesoscale eddy field (Callies et al. 2016). The slope tends to vary between $\alpha \approx 2$ in winter and $\alpha \approx 3$ in summer (Callies et al. 2015; Lawrence and Callies 2022). The only available way of studying the turbulence properties at a global scale is satellite altimetry, that measures the sea surface height (SSH). For motions that are in geostrophic balance, near-surface KE spectra $\mathcal{K}(k)$ convert to SSH variance spectra, $\mathcal{S}(k) = (f/gk)^2\mathcal{K}(k)$, where f is the local inertial frequency and g is the gravitational acceleration (Vallis 2017). KE spectra give rise to SSH spectral slopes $\alpha + 2$ that vary between about 4 and 5, indicating that the SSH signal associated with submesoscale turbulence is expected to be weak. It is estimated that even if presently available satellite altimetry data are pushed to their limit (e.g., Lawrence and Callies 2022), their resolution is ~100 km, such that an important part of the signal is drowned in noise. Furthermore, the SSH field at the mesoscale and below is a jigsaw puzzle of features due to geostrophically balanced turbulence and internal gravity waves. Distinguish between signals arising from these drastically different types of motion in order to correctly interpret the data is crucial and is still an open question for the largest part.

On the other hand, properties of the turbulence in the time domain (for frequencies ω, averaged over all wavenumbers) are less understood. Decades of studies have not yet found a consensus on the shape of the frequency spectrum for oceanic turbulence. The simplest model connecting the wavenumber and frequency domains is Taylor's hypothesis (Taylor 1938; Ferrari and Wunsch 2010; Arbic et al. 2012). This model predicts that the wavenumber and frequency slopes should be equal, which is clearly not the case from previous SSH observations and idealized simulations (Arbic et al. 2012). A dimensional argument by Tennekes and Lumley (1972), devised for three-dimensional, homogeneous turbulence but potentially applicable more generally, predicts a universal slope of the KE frequency spectrum equal to 2. However, following available in situ and satellite measurements, this argument does not hold either (de Marez et al. 2023). While the Taylor hypothesis fails, it is still likely that Doppler shifting shapes the frequency content at submesoscales. Callies et al. (2020) argued that the time scales registered by an Eulerian observer are substantially shorter than the time scales of Lagrangian evolution. The Doppler shifting will be more complicated than in Taylor's case if the dominant flow is a turbulent mesoscale eddy field.

In the present paper, we aim at providing an alternative to the usual description of the oceanic turbulence in the wavenumber domain. We present what we can learn about the ocean's geostrophic turbulence by looking at the time domain and essentially raise the question "What shapes the frequency spectrum of sea surface height?" The noise floor in the

Corresponding author: Charly de Marez, charly@hi.is

DOI: 10.1175/JPO-D-24-0113.1

frequency domain is small compared to wavenumber domain, and therefore, extracting balanced motions can be done by only considering frequencies below the inertial frequency—typically larger than the altimetric measurements Nyquist period, $\mathcal{O}(20)$ days. This allowed recent studies to successfully extract an estimate of the SSH frequency spectrum for balanced motions in the global ocean (de Marez et al. 2023), using *Jason-3* (*J3*) satellite measurement (Le Traon et al. 2017). Based on in situ measurements, these authors assumed that the frequency spectrum has a form

$$\mathcal{S}_\omega(\omega) = \frac{A_\omega}{1 + (\omega/\omega_0)^{s_\omega}}, \tag{1}$$

and they estimated its parameters: the amplitude A_ω, the transition frequency ω_0, and the slope s_ω. These parameters exhibit spatial patterns similar to the large and mesoscale energy levels (de Marez et al. 2023, and Fig. A1 in appendix A) suggesting that this spectrum is mainly influenced by the underlying balanced turbulence. Here, we refine the method described in de Marez et al. (2023). We first compute the wavenumber–frequency (k–ω) spectra along *J3* tracks. Properties of the SSH frequency spectrum are then extracted by fitting the model spectrum (1) on the marginal frequency spectrum (averaged over wavenumbers). When compared to quantities from ECCO reanalysis, we show that frequency spectra can be used as a proxy to understand the properties of the oceanic flow. When studying particular basins, different regimes coexist, depending on the regional dynamics. In particular, there is a relation, likely to be linear, between the slope of the frequency spectrum s_ω and the ratio of meridional potential vorticity gradients. This relation is found to match with the one observed in numerical simulations representing the oceanic turbulent field at the surface under the influence of Rossby waves. These results could be used to retrieve the oceanic surface properties from the frequency spectrum obtained with novel satellite altimetry—with more coverage and frequency sampling. We first present the spectral analysis from satellite data in section 2. We then analyze the frequency spectra in regard to a global reanalysis and numerical idealized simulations in sections 3 and 4 and finally with a simple theoretical model for Doppler shifting in section 5. We discuss our results in section 6.

2. Spectral analysis from satellite data

Refining a similar method as in de Marez et al. (2023), we use the along-track SSALTO/Data Unification and Altimeter Combination System (DUACS) Delayed-Time Level-3 SSH measurements made by the *Jason-3* altimeter (Le Traon et al. 2017) to estimate frequency spectra of SSH variance across the global ocean. The dataset consists of SSH time series along 254 tracks with ~7-km along-track spacing. The time series are 4 years long (2016–19) and have a spacing of 9.92 days. de Marez et al. (2023) computed frequency spectra from each SSH time series. Here, we rather compute the k–ω spectrum at each time series location, where k is computed along a 250-km-long segment in the along-track direction.

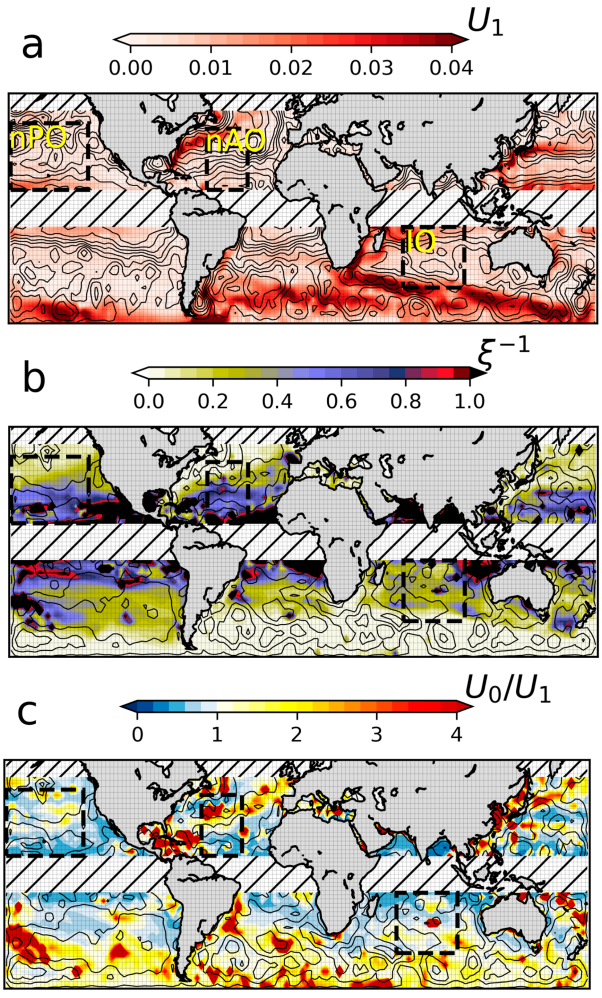

FIG. 1. (a) Modal amplitude of the first baroclinic mode (U_1; m s^{-1}), (b) ratio of meridional PV gradients (ξ^{-1}), and (c) ratio between the barotropic and first baroclinic modal amplitudes (U_0/U_1) derived from the ECCO reanalysis. In all maps, hatched areas show the equatorial and north polar areas that are excluded from the present analysis. Dashed line rectangles highlight the nPO, nAO, and IO areas. Contours in (a) show A_ω with $10^{0.2}$ m^2 cpd^{-1} spacing. Contours in (b) and (c) show s_ω = (2, 2.5, 3, 3.5). We refer the reader to Fig. A1 for color plots of A_ω and s_ω.

Hann windows are applied in the along-track and cross-track directions, and discrete Fourier transforms are taken giving a periodogram $|\hat{h}(k,\omega)|^2$ at each location between 60°S and 60°N. The resulting periodograms are then averaged over 2.5° × 2.5° boxes and finally integrated over wavenumbers to yield the SSH marginal frequency spectra. As in de Marez et al. (2023), we then assume that the SSH marginal frequency spectra have the form (1), and we re-estimate A_ω, ω_0, and s_ω in the global ocean by fitting this model spectrum (1) following the treatments and methods fully described in de Marez et al. (2023). These parameters exhibit patterns similar to the large and mesoscale energy levels (de Marez et al. 2023, and Figs. 1a,b) suggesting that this spectrum is mainly influenced by the underlying balanced turbulence.

The same method is applied on newly released Surface Water and Ocean Topography (SWOT, NASA/CNES) data, in particular the SWOT_L3_SSH dataset, derived from the L2 SWOT KaRIn low-rate ocean data products (NASA/JPL and CNES). It is produced and made freely available by AVISO and DUACS teams as part of the DESMOS Science team project (AVISO/DUACS 2023). We consider the 1-day repeat orbit stage of the mission spanning a 100 day period between 29 March 2023 and 9 July 2023. For each satellite pass, the data are displayed on a regular grid with 2-km spacing on the ~100-km swath. We compute SSH spectra for each grid point the same way as in *Jason-3* data and then average in the same 2.5° × 2.5° boxes. For the purpose of our study, we only considered passes 015, 028, 017, and 002, that pass by the North Pacific Ocean area. The advantage of this dataset is that 1) the 2D measure allows us to compute a lot of spectra at a given latitude, thus allowing a better spectral estimate for a unique satellite track, and 2) the 1-day repeat orbit allows us to extend the frequency spectral estimate to a frequency of 0.5 cpd.

3. Baroclinic instability as the source of mesoscale energy in the global ocean

The continuously stratified quasigeostrophic (QG) dynamics are described by the material conservation of the QG potential vorticity Q_{qg} (Vallis 2017) as

$$[\partial_t + \mathcal{J}(\Psi, \cdot)]Q_{\mathrm{qg}} = 0, \tag{2}$$

with

$$Q_{\mathrm{qg}} = \nabla^2\Psi + \beta y + \frac{\partial}{\partial_z}\left(\frac{f_0^2}{N^2}\frac{\partial}{\partial_z}\Psi\right), \tag{3}$$

where $\Psi(x, y, z, t)$ is the scalar 3D streamfunction, β is the local Rossby parameter, f_0 is the local Coriolis frequency, N is the Brunt–Väisälä frequency, and x, y, and z are the zonal, meridional, and vertical coordinates, respectively.

The streamfunction can be projected over normal vertical modes (Gill 1982; Tedesco et al. 2022) of vertical structure $h_n(z)$ as

$$\Psi(x, y, z, t) = \sum_{n=0}^{+\infty} \psi_n(x, y, t)h_n(z), \tag{4}$$

where

$$\frac{\partial}{\partial_z}\left(\frac{1}{N^2}\frac{\partial}{\partial_z}h_n\right) + \frac{1}{\lambda_n^2}h_n = 0, \tag{5}$$

with λ_n as the deformation radius of the nth mode, found by solving the eigenvalue problem [we hereafter define $\lambda_1 = R_D$, the first baroclinic deformation radius (Chelton et al. 1998)].

We use (5) to obtain the vertical decomposition of the velocity profile in the global ocean using the ECCO reanalysis data (ECCO Consortium et al. 2021). The data are displayed on a 0.5° × 0.5° grid, between 1992 and 2017 (in the following, all quantities are time averaged over this period). We then define a lower-resolution grid composed of 2.5° × 2.5° boxes. In each box, we average the stratification (N) profiles from ECCO and use (5) to obtain the 10 first vertical modes in this box. The eigenvalue problem is solved using the Python Dedalus library, with the same boundary condition as presented in Tedesco et al. (2022). This gives an estimate of h_n and λ_n for $0 \leq n \leq 10$. We then compute the amplitude of the normal modes of the velocity as

$$U_n = \frac{1}{H}\int_{-H}^{0} uh_n dz, \tag{6}$$

where u is the norm of the velocity profile on an ECCO-grid point, h_n is the nth vertical mode corresponding to the box the velocity profile is in, and H is the depth. Values of U_0 and U_1 as shown in Fig. 1 are box-averaged values (see an example of the different components of the modal decomposition in Fig. B1 in appendix B). This method allows us to take into account the variation of velocity within the box and also to be computationally efficient as we do not decompose into normal modes at each grid point.

We assume a zonal mean flow U with modal components U. Equation (2) becomes a system of n equations that we linearize around each component of the mean flow U_n (Vallis 2017). The meridional potential vorticity (PV) gradients for the first two equations $n = 0$ and $n = 1$ are $\Lambda_0 = \beta$ and $\Lambda_1 = U_1/R_D^2$, respectively. We call the PV gradient ratio $\xi = \Lambda_1/\Lambda_0$. If the ocean is mainly driven by the barotropic and first baroclinic components [i.e., truncate to $n = 0$ and $n = 1$ (Flierl 1978)], baroclinic instability (BCI) can occur if the meridional PV gradient changes sign vertically (Vallis 2017). This condition is equivalent to

$$\xi^{-1} = \frac{\beta R_D^2}{U_1} < 1. \tag{7}$$

This parameter sets the scale and the properties of the most unstable modes. Note that the case $\xi^{-1} = 0$ corresponds to f-plane dynamics and is always baroclinically unstable if $U_1 \neq 0$ (the flow has a baroclinic component).

Based on the ECCO reanalysis, it appears that $\xi^{-1} < 1$ in 85% of the ocean (excluding the equatorial band and polar regions, see Fig. 1b). Most of the ocean is unstable with respect to BCI and we observe a correspondence between instability to BCI and regions of high U_1: the turbulent energy in the ocean is most likely injected where U_1 is maximum (Fig. 1a), via BCI of major western boundary currents. This mostly coincides with places where A_ω is maximum (Fig. 1a): the energy content of SSH frequency spectra appears to be set by BCI, and this spectrum can be used to understand more thoroughly the turbulent characteristics of the ocean. In the following, we describe the different regimes that modulate the shape of the frequency spectrum in the specific areas defined in Fig. 1.

4. The ratio of meridional PV gradient as a control for the shape of the SSH frequency

a. *On the meridional variation of the observed SSH frequency slope*

We start by discussing the case study of the North Pacific Ocean (nPO) area. There, barotropic currents are weak (U_0/U_1

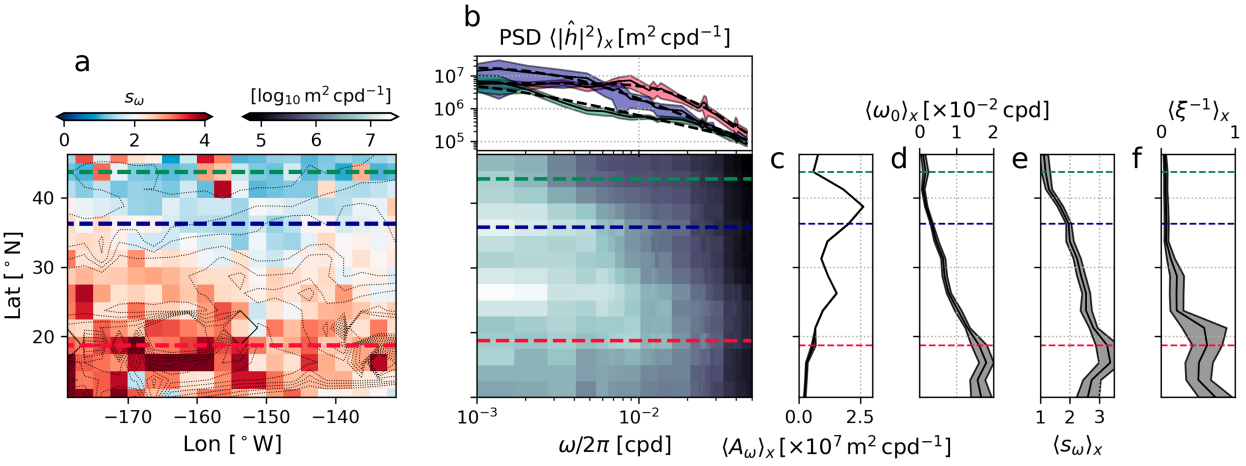

FIG. 2. Spectral analysis in the nPO area. (a) SSH frequency spectra slope s obtained from *J3*-data fits; contours show ξ^{-1}. (b) Zonally averaged *J3*-data frequency spectra as a function of latitude (bottom) and three particular examples at the latitudes showed in (a) (top); dashed lines show the fit of the model spectrum (1). (c)–(e) Parameters obtained from zonally averaged *J3*-data frequency spectrum fits (respectively, amplitude A, transition frequency ω_0, and slope s). (f) Zonally averaged ECCO-derived ξ^{-1}. Envelopes in all plots show the zonal standard deviation.

is small, Fig. 1c), the condition for baroclinic instability is satisfied everywhere ($\xi^{-1} < 1$, Fig. 1b), and the average first baroclinic component of current U_1 is ~0.01 m s^{-1} (Fig. 1a). The flow can thus be considered as a turbulent flow weakly influenced by external forcing, where energy is locally injected by the BCI of the first baroclinic component of the flow.

In this area, the slope of frequency spectra derived from satellite altimetry varies between $1 < s_\omega < 3.5$ (see Figs. 1, 2, and A1). The variation of spectral parameters is mainly meridional. We therefore compute the zonal average spectra (noted $\langle\cdot\rangle$) to study the dynamics at a given latitude (see Figs. 2b and 3). The model spectrum (1) successfully captures the shape of low-frequency spectra below ~40°N (see e.g., Figs. 3a and 3b). Spectra computed using the higher temporal resolution SWOT data show that the spectral amplitude as well as the model spectrum fit are correctly estimated down to the *J3*-data Nyquist frequency ($\omega/2\pi \sim 4 \times 10^{-2}$ cpd). At higher latitudes, staircase-like spectra are measured (see e.g., Fig. 3c). *J3*- and SWOT-derived spectra amplitudes also do not match. The description of such spectra is beyond the scope of the present paper, but we could argue that at these latitudes, the spectra are influenced by nonlocal phenomena, e.g., topographic, coastal currents, or zonal Rossby waves jets.

Spectral parameters vary with latitude, with a poleward increase of $\langle A_\omega\rangle_x$ and a poleward decrease of $\langle\omega_0\rangle_x$ and $\langle s\omega\rangle_x$ (Figs. 2c–e). The variation of the Coriolis frequency with latitude (set by β) in such areas where U_1 varies little induces a strong meridional change of $\langle\xi^{-1}\rangle_x$ (Fig. 2f). Below ~38°N, the slope of the frequency spectrum $\langle s\omega\rangle_x$ varies meridionally together with $\langle\xi^{-1}\rangle_x$, with $\langle s\omega\rangle_x \sim 3$ at low latitude where $\langle\xi^{-1}\rangle_x \sim 0.6$ and $\langle s\omega\rangle_x \sim 2$ where $\langle\xi^{-1}\rangle_x \to 0$ (see Fig. 4a). This meridional variation is also seen for *J3*-measured spectra in the Indian Ocean (IO) area, where all considered data points are far from coastlines and north of the ACC signature

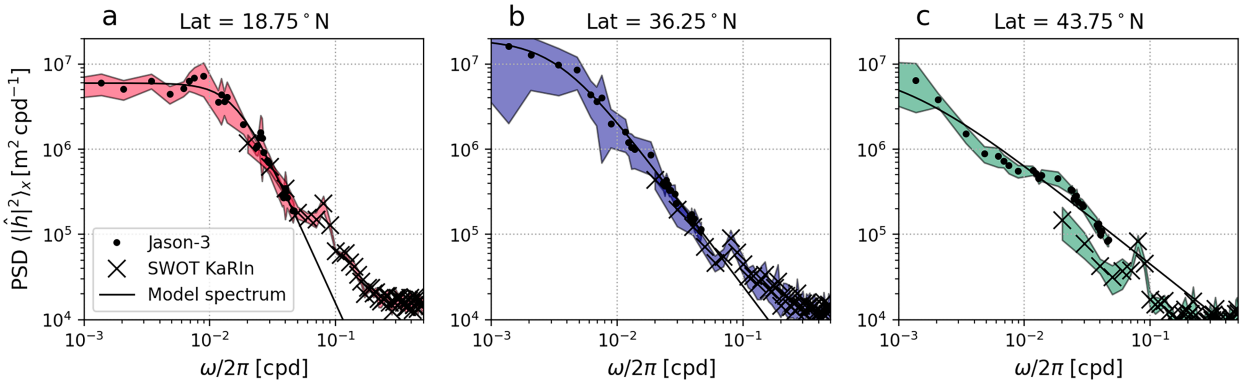

FIG. 3. (a)–(c) The zonally averaged SSH frequency spectrum from *J3* data (dots) to SWOT KaRIn (crosses) time series at three different latitudes in the nPO area; color envelopes show the standard deviation of spectra; solid line shows the fit of the model spectrum over the *J3* data [$\langle s_\omega\rangle_x = 3.26, 1.96, 1.17 \pm 0.19, 0.04, 0.07$ for (a)–(c), respectively].

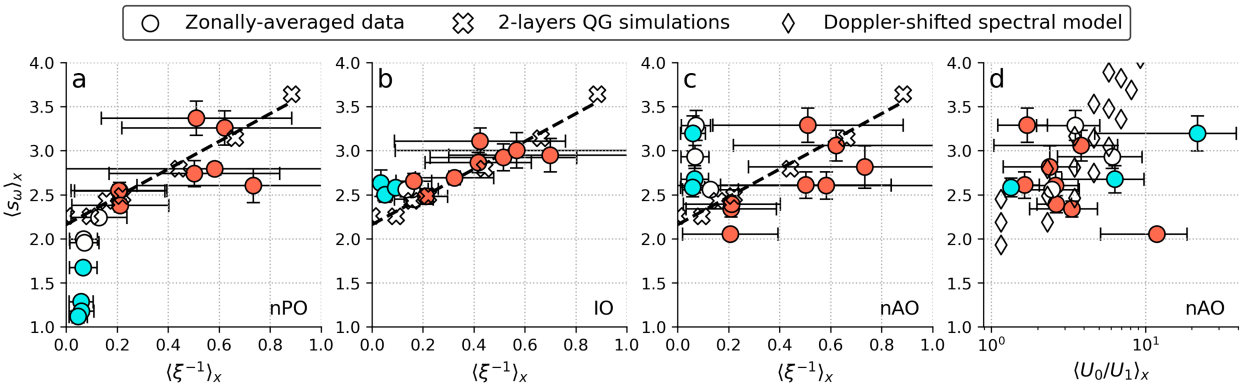

FIG. 4. (a) [respectively, (b),(c)] Zonally averaged SSH frequency spectra slope s_ω obtained from *J3*-data fits in the nPO (respectively, IO and nAO) area as a function of zonally averaged ECCO-derived ξ^{-1}; color indicates the latitude (red: lat $< 30°$, white: $30° <$ lat $< 38°$, blue: lat $> 38°$); crosses show the SSH frequency spectra slope in the two-layer QG simulation with a given ξ^{-1}; dashed line show a linear fit of simulation $s_\omega = f(\xi^{-1})$. (d) Zonally averaged SSH frequency spectra slope s_ω obtained from *J3*-data fits in the nAO area as a function of ECCO-derived U_0/U_1; diamonds show the slope of Doppler-shifted spectra by a given barotropic current with values U_0/U_1 for the frequency spectrum model (with slope $s_\omega^0 = [1.75, 2, 2.25]$). Error bars indicate the zonal standard deviation.

(Figs. 1 and 4b). In this area, the scaling appears to follow a linear trend. In the North Atlantic Ocean (nAO), data points measured below ~30°N (i.e., far from the Gulf Stream) also follow this trend, despite the spreading due to the small zonal extension of the area (see Figs. 1c and 4c).

b. *Numerical model*

The analysis of *J3* data suggest that at midlatitudes, where $\xi^{-1} \sim 0$, the SSH frequency slope tends to $s_\omega = 2$ (Fig. 4). A frequency spectrum following a constant drop-off with slope $s_\omega = 2$ is typical of expectations for a turbulent flow on an f plane (Taylor 1938; Tennekes and Lumley 1972; Ferrari and Wunsch 2010; Arbic et al. 2012; Callies et al. 2020). If the local dynamics have time scale $T > 1$ day, length scale $L > R_D$, and its major dynamical components are the barotropic and first baroclinic modes, the ocean can be fairly well modeled by two-layer QG dynamics (Flierl 1978).

To further understand the underlying mechanism leading to change in frequency spectra, we make use of a QG model based on the framework and numerical methods described in Callies et al. (2016), in a nondimensionalized two-layer version, to run simulations of forced turbulence. It consists of a doubly periodic domain, with a surface layer (subscript 1) in the rigid lid approximation and a bottom layer (subscript 2) with no bottom friction, whose respective thicknesses are h_1 and h_2, thus defining the aspect ratio $\delta = h_1/h_2$. We impose a mean baroclinic zonal flow $\mathbf{U} = (U, -U)$, that sets the mean vertical gradient of potential vorticity. Quantities are nondimensionalized such that $x, \sim R_D$, $u, v \sim U$, and $t \sim R_D/U$ with R_D as the first baroclinic radius of deformation. This way, the model solves the nondimensional equations:

$$\partial_t q_i + \mathcal{J}(\psi_i, q_i) \pm \partial_x q_i + (\beta^* \mp F_i)\partial_x \psi_i = r\nabla^{-2} q_i - \nu(-\nabla^2)^n q_i, \tag{8}$$

for $i = 1, 2$, with ψ_i as the streamfunction anomaly, q_i as the potential vorticity anomaly, β^* as the nondimensional Rossby parameter, $\mathcal{J}$ as the Jacobian operator, $F_1 = 1/(1 + \delta)$, and $F_2 = \delta/(1 + \delta)$. We integrate these equation on a 128×128 points grid, with time steps adjusted to respect the CFL criterion. Small scales are damped through hyperviscosity of order $n = 10$ coefficient ν and large scales through hypoviscosity coefficient r. The ratio of the meridional gradient of potential vorticity in its nondimensional quasigeostrophic form is

$$\xi^{-1} = \beta^*(\delta + 1)/\delta, \tag{9}$$

which can be directly compared to its dimensional definition (7).

In this framework, the only parameters that vary are U, R, ξ^{-1}, r, and ν. We adjust these parameters so the simulations represent the nPO area: we set $U = 0.04$ m s^{-1} and $R_D = 15$ km, which corresponds to the value of $\langle U_1 \rangle_x$ and $\langle R_D \rangle_x$ from ECCO data at 36°N in the nPO area (see Fig. 1). The value of ν is chosen so it is as small as possible for the simulation not to blow up and minimally affects the mesoscale dynamics discussed below. Then, starting with the f-plane ($\xi^{-1} = 0$) case, r is chosen so that the simulated rescaled frequency spectrum has the same energy content (A_ω and ω_0) than the *J3*-derived frequency spectrum at 36°N (Fig. 3b). For cases with $\xi^{-1} \neq 0$, we retune r such that the domain-integrated KE when the turbulence is at equilibrium is the same in all simulations.

These simulations are designed to represent a forced turbulence flow at midlatitudes as is observed in *J3* satellite measurements. The energy in the simulations is injected via BCI of the mean current because the meridional gradients of potential vorticity for the two layers have opposite signs. The growth rate of the instability is maximum at a scale of ~100 km, with a value of 0.07 days^{-1} (see Fig. 5a). This leads to an exponential increase of KE during the first months of the simulation (see Fig. 5b). Energy subsequently cascades toward larger scales, and it is dissipated at the domain scale (~1000 km) by hypoviscosity. After a few simulated months, the KE reaches an equilibrium that lasts throughout the entire simulation (here 10 years), see Fig. 5b. We only consider this equilibrium

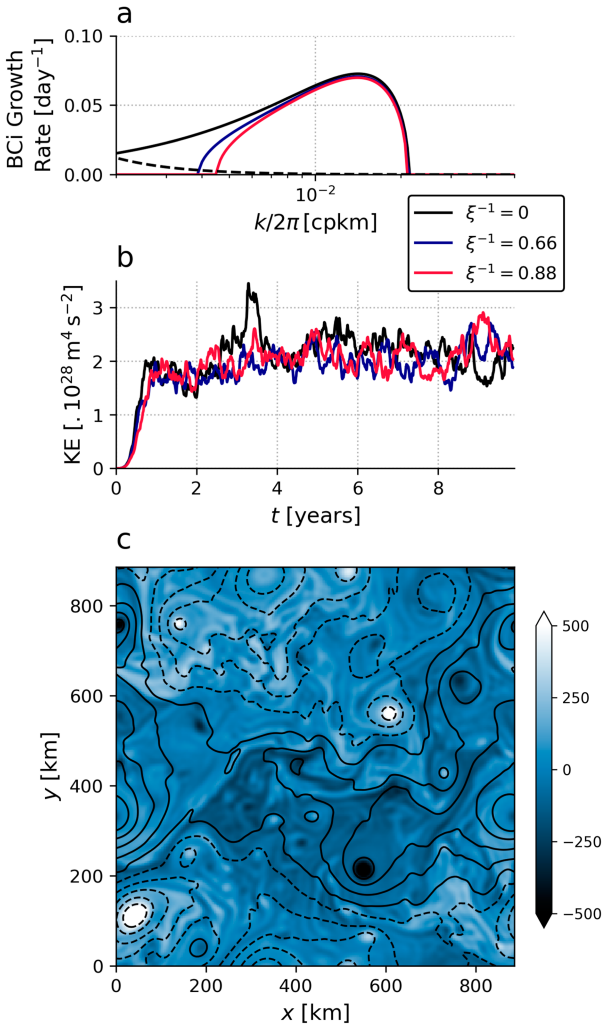

FIG. 5. (a) Growth rate of the most unstable modes for the primary BCI following linear stability calculation; dashed line shows the damping rate from hypoviscosity. (b) Integrated KE evolution in the two-layer QG simulation. (c) Snapshot of PV in the surface layer for the $\xi^{-1} = 0$ simulation (in nondimensionalized model units); contours show the streamfunction. In (a) and (b), color indicates the simulation considered (see legend).

state for our further analysis. It represents the midlatitude mesoscale dynamics captured by *J3* satellite measurements: the flow consists of $\mathcal{O}(100)$ km eddies and mesoscale fronts (see Fig. 5c).

We compute SSH frequency spectra from the output streamfunction and fit the model spectrum (1) in the frequency band covered by *J3* data. For $\xi^{-1} = 0$ (f-plane case), the simulation reproduces a SSH frequency spectrum with a slope $s_\omega = 2$ that matches *J3*-derived spectrum (see Fig. 6a) and a SSH wavenumber spectrum with a slope of 5 (see Fig. 6b). When modifying ξ^{-1}, the slope of the SSH wavenumber spectrum does not change: there is no change in spectral properties of the turbulence if analyzing only the wavenumber spectra (see Fig. 6b). On the other hand, we observe a steepening of the SSH frequency spectra when ξ^{-1} increases. For these cases, the barotropic meridional gradient of potential vorticity is nonnull, and it supports the propagation of Rossby waves in the domain. The more energetic ones are at the domain scale and therefore sign as high variance patches in the SSH k–ω spectrum at the lowest wavenumbers and at frequencies set by their dispersion relation, here for $3 \times 10^{-3} \lesssim \omega/2\pi \lesssim 10^{-2}$ cpd (Fig. 6c). These Rossby waves then appear in the marginal frequency spectrum (i.e., integrated over wavenumbers) in the form of a variance increase at $\omega \sim 10^{-2}$ cpd (Fig. 6d). This leads to a steepening of the frequency spectrum at the highest frequencies. Quantitatively, the slope of the simulated SSH frequency spectra s_ω increases together with ξ^{-1}. The $s_\omega(\xi^{-1})$ follows a linear trend,

$$s_\omega = a_0 \times \xi^{-1} + a_1, \tag{10}$$

with $a_0 = 1.57 \pm 0.10$ and $a_1 = 2.16 \pm 0.04$, which compares favorably with zonally averaged *J3*-derived values discussed in the previous section at midlatitudes (Figs. 4a–c). This demonstrates that the shape of the SSH frequency spectra is set by this meridional change of background potential vorticity gradient.

5. Impact of local barotropic currents on the frequency spectrum

In many areas, the barotropic component of the flow is at least as intense as the baroclinic one, i.e., $U_0/U_1 > 1$ (see Fig. 1c). This is the case in the northernmost part of the nAO area, above ~30°N. At these locations, $\xi^{-1} \sim 0$, but the frequency spectra slopes nonetheless vary between $2.5 < s_\omega < 3.5$ (Fig. 4c). The larger U_0/U_1, the larger the zonal standard deviation, but nevertheless, $\langle s_\omega \rangle_x$ appears to roughly increase together with $\langle U_0/U_1 \rangle$ (see Fig. 4d). Even if only a small number of data points are available, a possible explanation for this would be that the barotropic current induces a Doppler shifting that will steepen the SSH frequency spectrum: the larger U_0/U_1, the larger s_ω.

We estimate this effect with a model spectrum for the SSH for which the marginal frequency spectrum has a slope s_ω^0. We use the k–ω model spectrum

$$\mathcal{S}(k, \omega) = \frac{A}{[1 + (k/k_0)^a + (\omega/\omega_0)^b]^c} \tag{11}$$

to represent the SSH variance of background balanced turbulence (de Marez et al. 2023). The A sets the overall amplitude of the spectrum; k_0 and ω_0 set the wavenumber and frequency at which the spectrum transitions from a plateau at low frequencies and wavenumbers to a power-law drop-off; and a, b, and c control both the shape of this transition and the behavior at high wavenumbers and frequencies. Here, k is an along-track wavenumber, not the magnitude of a two-dimensional wavenumber vector. The model spectrum (11) is similar to the one proposed in Wortham and Wunsch (2014)—with a key difference which is the nonseparable form of the power law. de Marez et al. (2023) showed using in situ data that the nonseparability, the power-law behavior at high frequencies/wavenumbers, and the plateau at low frequencies/wavenumbers

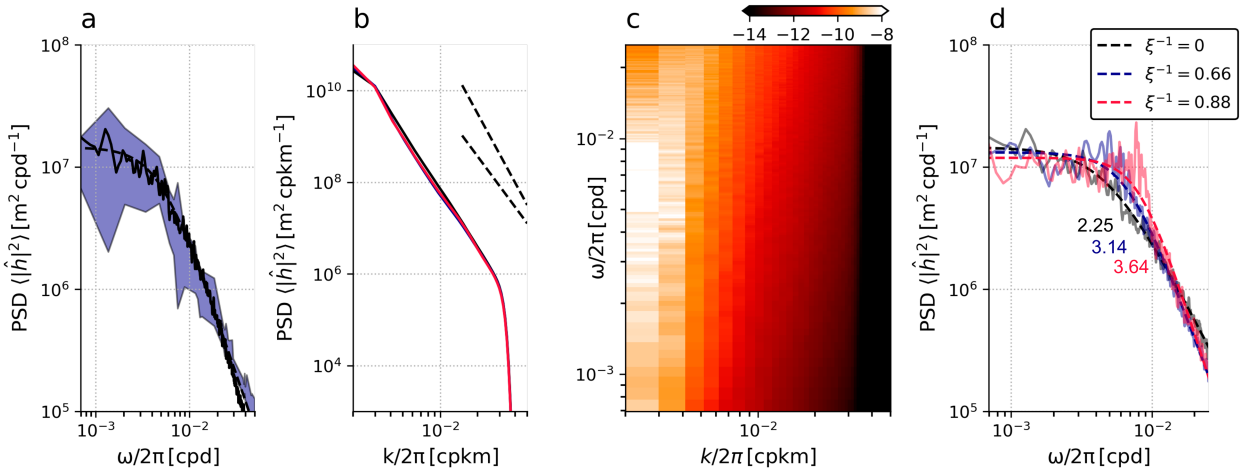

FIG. 6. (a) The SSH marginal frequency spectrum of the $\xi^{-1} = 0$ (f-plane) simulation (solid line) and its fit using the model spectrum (1) (dashed line); blue envelope shows *J3*-data frequency spectrum at 36.25°N (same as in Fig. 3b). (b) SSH marginal wavenumber spectra in the $\xi^{-1} = 0$, 0.66, and 0.88 simulations; dashed lines show the $k^{-11/3}$ and k^{-5} slopes. (c) SSH k–ω spectrum in the $\xi^{-1} = 0.88$ simulation. (d) SSH marginal frequency spectra in the $\xi^{-1} = 0$, 0.66, and 0.88 simulations, and their fit using the model spectrum (1); the respective values of s_ω are shown in color next to the fits. In (b) and (d), color indicates the simulation considered (see legend).

of the model (11) accurately constrain the variance of balanced motions for the SSH. If we impose that the frame of reference—in which $\mathcal{S}(k, \omega)$ defines the SSH variance—moves at a velocity u_0 in the along-track direction, an Eulerian (nonmoving) observer will measure a Doppler-shifted spectrum

$$\mathcal{S}'(k, \omega) = \frac{A}{[1 + (k/k_0)^a + (\omega'/\omega_0)^b]^c}, \tag{12}$$

with $\omega' = \omega - u_0 k$.

The spectral slope s, in the high-frequency limit for a Doppler-shifted turbulent flow, can be estimated after integrating (12) over wavenumbers (giving the marginal frequency spectrum of amplitude A_ω). The result depends on several parameters. We set $k_0 = 2\pi/250$ cpkm, as it fairly well represents the mesoscale turbulence activity at midlatitudes (Lawrence and Callies 2022; de Marez et al. 2023). Also, A_ω and ω_0 are chosen as median values in the nAO area: $A_\omega = 6.7 \times 10^6$ m^2 cpd^{-1} and $\omega_0 = 3.8 \times 10^{-2}$ cpd. We choose to set $c = 1$ as it merely controls the behavior near the transition between the plateau and power-law range and has little impact on the present results (de Marez et al. 2023). The a and b are related to marginal spectra slopes following

$$a = \frac{s_k s_\omega - 1}{s_\omega - 1} \quad \text{and} \quad b = \frac{s_k s_\omega - 1}{s_k - 1}. \tag{13}$$

They are chosen such that the spectrum integrated over frequencies (the marginal wavenumber spectrum) has a slope $s_k = 5$ (consistent with the typical drop-off of turbulent oceanic flow, Callies et al. 2015), knowing that s_ω^0 sets the slope of the frequency spectrum in the moving frame of reference. A sensitivity analysis showed that slightly changing all these parameters minimally affects the present results.

For a given set of parameters $(k_0, \omega_0, s_k, s_\omega^0)$, we can vary the mean current u_0, compute the marginal frequency spectrum, and measure the slope s_ω in the Eulerian frame of reference using a least squares fit of the function (1) in the same frequency range as in satellite *J3* data (see Fig. 7a). If we suppose that the background turbulent flow is driven by baroclinic instability, $\tilde{u}_0 = u_0 \times k_0/\omega_0$ is equivalent to the ratio U_0/U_1 measured in ECCO data. For the range of parameters observed in the nAO area, i.e., $u_0 = [0, 0.02, 0.04, 0.08, 0.1]$ m s^{-1} ($\tilde{u}_0 = [0, 1.2, 2.3, 3.5, 4.6]$ in its dimensionless form), the slope increases linearly from $s_\omega = 2.0$ at $\tilde{u}_0 = 0$ to $s_\omega = 3.14$ at $\tilde{u}_0 = 4.6$ (Figs. 7a,b). This theoretical estimate, assuming $s_\omega^0 = [1.75, 2.0, 2.25]$, falls within error bars of zonally averaged *J3*-derived values for s_ω (Fig. 4d). This supports the fact that the steepening of the frequency spectrum as U_0/U_1 increases is mostly due to the Doppler shifting of background BCI-driven turbulence.

6. Discussion

In most of the ocean, the flow can be decomposed into barotropic and baroclinic components. The ratio of the PV gradients associated with each of them (ξ^{-1}) and the associated zonal mean currents ratio (U_0/U_1) vary. Interpreting the frequency spectrum shape is therefore challenging and it needs to be done knowing the regional dynamical properties. In the South Pacific Ocean, for example, the South Pacific Current and the proximity with the Subantarctic Front of the Antarctic Circumpolar Current lead to a strong barotropic component of the velocity. These currents are east-oriented, thus canceling the Doppler shifting of the frequency spectrum by Rossby waves, and subsequently leading to a rather constant value of slope $s_\omega \approx 2$ in this basin (Fig. 1b). In western boundary systems such as the Kuroshio Extent, the Gulf Stream, and the Agulhas Current regions, slope values are far from

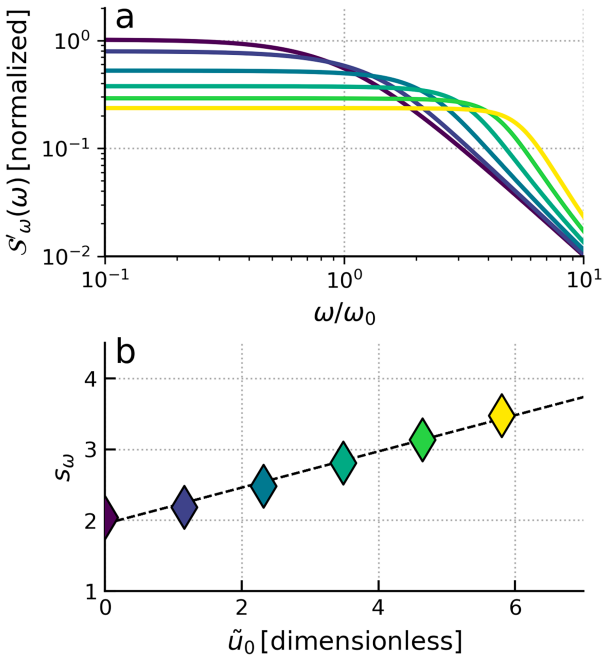

FIG. 7. (a) The marginal frequency spectrum $\mathcal{S}'_\omega(\omega)$, when the background turbulent flow is advected by a mean current $\tilde{u}_0$ [color coding is for $\tilde{u}_0$; see (b)]; spectra are normalized by the amplitude of $\mathcal{S}'_\omega(\omega)$ for $u_0 = 0$. (b) Variation of the slope for a model spectrum of the form (1), for the same values of u_0 as in (a); linear least squares fit is shown by dashed lines.

open ocean results, reaching $s_\omega > 3.5$ (Fig. 1b). At these locations, the arguments developed in this study are not applicable because 1) the turbulence is not fully developed (the flow mainly consists of large/intense laminar currents) and 2) the proximity of the coast prevents the turbulence to reach equilibrium by injecting energy in the system (Waterman and Jayne 2011). Frequency spectra steepness is most likely due to the signature of slowly varying currents, that fill the spectrum at low frequencies. Remotely generated mesoscale vortices, such as Gulf Stream Rings (Richardson 1983) and Agulhas Rings (Olson and Evans 1986), can also significantly steepen frequency spectra. In the South Atlantic Ocean, for instance, drifting Agulhas rings have an external radius of ~100–400 km and a drifting speed of ~5–8 cm s^{-1} (Laxenaire et al. 2019). The passage of such eddies thus have a frequency signature between $\sim 5 \times 10^{-3}$ cpd and $\sim 2 \times 10^{-2}$ cpd. This leads to broad peaks in the frequency spectrum at these frequencies (not shown), that subsequently fill the spectrum, and increase the spectral slope.

7. Conclusions

Our findings suggest that far from the influence of planetary Rossby waves and strong barotropic currents, the large to mesoscale balanced turbulence is likely to produce SSH frequency spectra with slope $s_\omega \approx 2$. This is in agreement with previous studies (Arbic et al. 2012), and it is a first step in understanding the conversion from wavenumber to frequency domains for SSH variance. Elsewhere, if the barotropic component of the flow can be neglected, planetary Rossby waves propagate in the domain and steepen the frequency spectrum at high frequencies. This can be quantitatively described by two-layer QG dynamics: the frequency spectrum slope scales—linearly—with the local value of ξ^{-1}. Where the barotropic current cannot be neglected, the steepening of the frequency spectrum can be fairly well predicted by assuming that the flow is Doppler-shifted by the local current.

Contrary to the classical wavenumber approach, the study of frequency spectrum implies a good knowledge of the local dynamics of the basin the frequency spectrum is measured in: frequency spectrum properties can exhibit complicated patterns due to entangled dynamics. Despite this, this gives a unique chance to study the properties of oceanic turbulence if 1) the wavenumber spectrum is not measurable or 2) the information given by wavenumber spectrum are not enough to understand the underlying phenomena.

Altogether, these results show that with further work, the study of the frequency spectrum of SSH as observed by satellite could be an efficient tool in retrieving the properties of the oceanic turbulence. In the context of upcoming high-resolution satellite mission, this framework will complement the study of wavenumber spectra and will allow retrieval of the turbulence properties in the open ocean and, therefore, to better assess on a global scale heat, CO_2, and other tracer exchanges in the global ocean.

Acknowledgments. C. d. M. was supported by NASA Grant 80NSSC20K1140 during the study and by a Queen Margrethe II's and Vigdís Finnbogadóttir's Interdisciplinary Research Centre on Ocean, Climate, and Society (ROCS) postdoctoral fellowship during the finalization of the writting. J. C. was supported by NASA Grant 80NSSC20K1140.

Data availability statement. Sea surface height *Jason-3* data are distributed by AVISO+ with support from CNES and can be downloaded on Copernicus data access service (https://data.marine.copernicus.eu/product/SEALEVEL_GLO_PHY_L3_MY_008_062/services). SWOT_L3_SSH dataset is produced and made freely available by AVISO and DUACS teams as part of the DESMOS Science team project (AVISO/DUACS 2023). It is available on AVISO website (https://www.aviso.altimetry.fr/en/data/products/sea-surface-height-products/global/swot-l3-ocean-products.html). ECCO reanalysis data were obtained on PODAAC website (https://podaac.jpl.nasa.gov/dataset/ECCO_L4_TEMP_SALINITY_05DEG_MONTHLY_V4R4). The QG model is available on author's GitHub (https://github.com/joernc/QGModel). Scripts and data to reproduce the study are available on the author's GitHub (https://github.com/demarez/freqspectrum).

APPENDIX A

Spectral Parameters from *Jason-3* Time Series

Figure A1 recalls the spectral parameters found in de Marez et al. (2023).

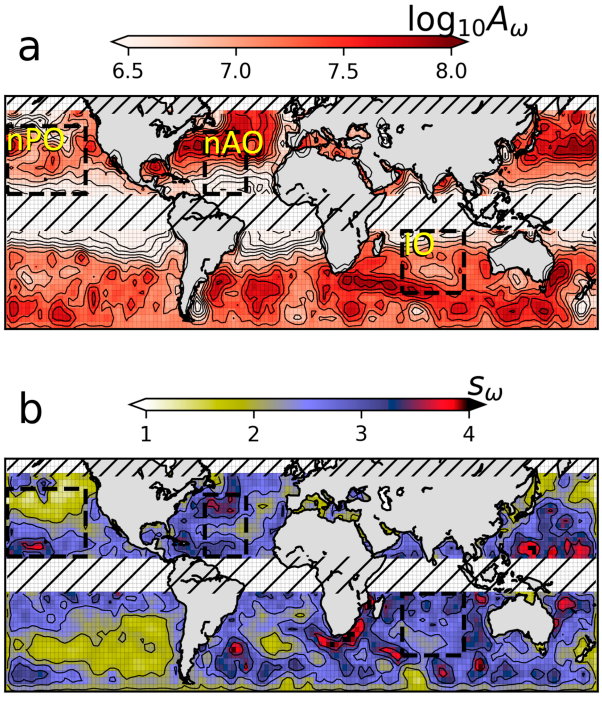

FIG. A1. (a) Spectral amplitude A_ω. (b) Spectral slope s_ω. The same contours as in Fig. 1 are shown.

APPENDIX B

Modal Decomposition in the Gulf Stream

Figure B1 shows an example of modal decomposition in the Gulf Stream area using the ECCO reanalysis.

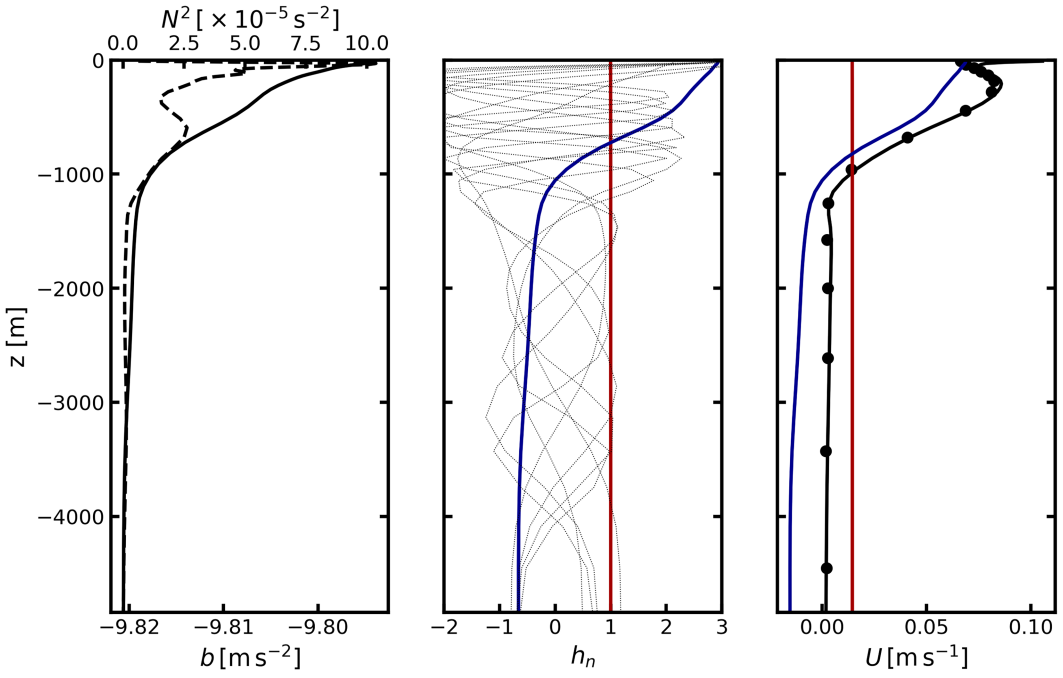

FIG. B1. Example of modal decomposition of the current profile in the Gulf Stream area. (left) Solid (respectively, dashed) line shows the time and box-averaged Brunt–Väisälä frequency (respectively, buoyancy) from the ECCO reanalysis. (middle) First 10 vertical modes obtained by solving six using the stratification shown in left panel; red and blue lines show the barotropic and first baroclinic modes, respectively. (right) Black line shows the time and box-averaged current profile in the same area from the ECCO reanalysis; the barotropic and first baroclinic projections of the velocity profile are shown in red and blue, respectively; black dots show the sum of the 10 first modes, reconstructing the total current profile.

REFERENCES

Arbic, B. K., R. B. Scott, G. R. Flierl, A. J. Morten, J. G. Richman, and J. F. Shriver, 2012: Nonlinear cascades of surface oceanic geostrophic kinetic energy in the frequency domain. *J. Phys. Oceanogr.*, **42**, 1577–1600, https://doi.org/10.1175/JPO-D-11-0151.1.

AVISO/DUACS, 2023: SWOT Level-3 SSH, SWOT_L3_SSH['basic'] (version 0.3). Accessed 9 January 2024, https://doi.org/10.24400/527896/A01-2023.017.

Beal, L. M., W. P. M. De Ruijter, A. Biastoch, R. Zahn, and SCOR/WCRP/IAPSO Working Group 136, 2011: On the role of the Agulhas system in ocean circulation and climate. *Nature*, **472**, 429–436, https://doi.org/10.1038/nature09983.

Callies, J., and R. Ferrari, 2013: Interpreting energy and tracer spectra of upper-ocean turbulence in the submesoscale range (1–200 km). *J. Phys. Oceanogr.*, **43**, 2456–2474, https://doi.org/10.1175/JPO-D-13-063.1.

——, ——, J. M. Klymak, and J. Gula, 2015: Seasonality in submesoscale turbulence. *Nat. Commun.*, **6**, 6862, https://doi.org/10.1038/ncomms7862.

——, G. Flierl, R. Ferrari, and B. Fox-Kemper, 2016: The role of mixed-layer instabilities in submesoscale turbulence. *J. Fluid Mech.*, **788**, 5–41, https://doi.org/10.1017/jfm.2015.700.

——, R. Barkan, and A. N. Garabato, 2020: Time scales of submesoscale flow inferred from a mooring array. *J. Phys. Oceanogr.*, **50**, 1065–1086, https://doi.org/10.1175/JPO-D-19-0254.1.

Chelton, D. B., R. A. deSzoeke, M. G. Schlax, K. El Naggar, and N. Siwertz, 1998: Geographical variability of the first baroclinic Rossby radius of deformation. *J. Phys. Oceanogr.*, **28**, 433–460, https://doi.org/10.1175/1520-0485(1998)028<0433:GVOTFB>2.0.CO;2.

de Marez, C., J. Callies, B. Haines, D. Rodriguez-Chavez, and J. Wang, 2023: Observational constraints on the submesoscale sea surface height variance of balanced motion. *J. Phys. Oceanogr.*, **53**, 1221–1235, https://doi.org/10.1175/JPO-D-22-0188.1.

ECCO Consortium, I. Fukumori, O. Wang, I. Fenty, G. Forget, P. Heimbach, and R. M. Ponte, 2021: Synopsis of the ECCO Central Production global ocean and sea-ice state estimate, Version 4 Release 4. Zenodo, accessed 6 October 2022, https://doi.org/10.5281/ZENODO.3765928.

Ferrari, R., and C. Wunsch, 2010: The distribution of eddy kinetic and potential energies in the global ocean. *Tellus*, **62A**, 92–108, https://doi.org/10.3402/tellusa.v62i2.15680.

Flierl, G. R., 1978: Models of vertical structure and the calibration of two-layer models. *Dyn. Atmos. Oceans*, **2**, 341–381, https://doi.org/10.1016/0377-0265(78)90002-7.

Gill, A. E., 1982: *Atmosphere-Ocean Dynamics*. Vol. 30. Academic Press, 662 pp.

Lawrence, A., and J. Callies, 2022: Seasonality and spatial dependence of mesoscale and submesoscale ocean currents from along-track satellite altimetry. *J. Phys. Oceanogr.*, **52**, 2069–2089, https://doi.org/10.1175/JPO-D-22-0007.1.

Laxenaire, R., S. Speich, and A. Stegner, 2019: Evolution of the thermohaline structure of one Agulhas Ring reconstructed from satellite altimetry and Argo floats. *J. Geophys. Res. Oceans*, **124**, 8969–9003, https://doi.org/10.1029/2018JC014426.

Le Traon, P.-Y., G. Dibarboure, G. Jacobs, M. Martin, E. Rémy, and A. Schiller, 2017: Use of satellite altimetry for operational oceanography. *Satellite Altimetry over Oceans and Land Surfaces*, D. Stammer and A. Cazenave, Eds., CRC Press, 581–608.

Olson, D. B., and R. H. Evans, 1986: Rings of the Agulhas current. *Deep-Sea Res.*, **33A**, 27–42, https://doi.org/10.1016/0198-0149(86)90106-8.

Palter, J. B., 2015: The role of the Gulf Stream in European climate. *Annu. Rev. Mar. Sci.*, **7**, 113–137, https://doi.org/10.1146/annurev-marine-010814-015656.

Richardson, P. L., 1983: Gulf Stream rings. *Eddies in Marine Science*, A. R. Robinson, Ed., Springer, 19–45, https://doi.org/10.1007/978-3-642-69003-7_2.

Small, R. J., and Coauthors, 2008: Air–sea interaction over ocean fronts and eddies. *Dyn. Atmos. Oceans*, **45**, 274–319, https://doi.org/10.1016/j.dynatmoce.2008.01.001.

Taylor, G. I., 1938: The spectrum of turbulence. *Proc. Roy. Soc. London*, **164A**, 476–490, https://doi.org/10.1098/rspa.1938.0032.

Tedesco, P., J. Gula, P. Penven, and C. Ménesguen, 2022: Mesoscale eddy kinetic energy budgets and transfers between vertical modes in the Agulhas Current. *J. Phys. Oceanogr.*, **52**, 677–704, https://doi.org/10.1175/JPO-D-21-0110.1.

Tennekes, H., and J. L. Lumley, 1972: *A First Course in Turbulence*. MIT Press, 320 pp.

Vallis, G. K., 2017: *Atmospheric and Oceanic Fluid Dynamics*. Cambridge University Press, 946 pp.

Villas Bôas, A. B., L. Lenain, B. D. Cornuelle, S. T. Gille, and M. R. Mazloff, 2022: A broadband view of the sea surface height wavenumber spectrum. *Geophys. Res. Lett.*, **49**, e2021GL096699, https://doi.org/10.1029/2021GL096699.

Waterman, S., and S. R. Jayne, 2011: Eddy-mean flow interactions in the along-stream development of a western boundary current jet: An idealized model study. *J. Phys. Oceanogr.*, **41**, 682–707, https://doi.org/10.1175/2010JPO4477.1.

Wortham, C., and C. Wunsch, 2014: A multidimensional spectral description of ocean variability. *J. Phys. Oceanogr.*, **44**, 944–966, https://doi.org/10.1175/JPO-D-13-0113.1.

Zhai, X., H. L. Johnson, and D. P. Marshall, 2010: Significant sink of ocean-eddy energy near western boundaries. *Nat. Geosci.*, **3**, 608–612, https://doi.org/10.1038/ngeo943.

Zhang, Z., W. Wang, and B. Qiu, 2014: Oceanic mass transport by mesoscale eddies. *Science*, **345**, 322–324, https://doi.org/10.1126/science.1252418.